

MOCK: an Algorithm for Learning Nonparametric Differential Equations via Multivariate Occupation Kernel Functions

Victor Rielly

*Department of Mathematics
Portland State University*

victor23@pdx.edu

Kamel Lahouel

Translational Genomics Research Institute

klahouel@tgen.org

Ethan Lew

ethanlew16@gmail.com

Michael Wells

*Department of Mathematics
Portland State University*

mlwells@pdx.edu

Vicky Haney

*Department of Mathematics
Portland State University*

vhaney@pdx.edu

Bruno Jedynak

*Department of Mathematics
Portland State University*

bjedyna2@pdx.edu

Abstract

Learning a nonparametric system of ordinary differential equations from trajectories in a d -dimensional state space requires learning d functions of d variables. Explicit formulations often scale quadratically in d unless additional knowledge about system properties, such as sparsity and symmetries, is available. In this work, we propose a linear approach, the multivariate occupation kernel method (MOCK), using the implicit formulation provided by vector-valued reproducing kernel Hilbert spaces. The solution for the vector field relies on multivariate occupation kernel functions associated with the trajectories and scales linearly with the dimension of the state space. We validate through experiments on a variety of simulated and real datasets ranging from 2 to 1024 dimensions. MOCK outperforms all other comparators on 3 of the 9 datasets on full trajectory prediction and 4 out of the 9 datasets on next-point prediction.

1 Introduction

1.1 Description of the problem

The task of learning dynamical systems derived from ordinary differential equations (ODEs) has garnered a lot of interest in the past couple of decades. In this framework, we are often provided noisy data from trajectories representative of the dynamics we wish to learn, and we provide a candidate model to describe the dynamics. We present a learning algorithm for the vector field guiding the dynamical system that scales linearly with the dimensionality of the dynamical system's state space.

1.2 State of the art

We compare MOCK to various dynamical systems learning methods, including sparse identification of nonlinear dynamics, reduced order models, deep learning methods, and neural ODEs. These methods learn system dynamics from trajectories in the state space with good accuracy, scale to tens, hundreds, or thousands of state dimensions, and are robust to noise. A detailed description of the comparators is presented in section 4.4 and in appendix G.

1.3 Main contributions

We propose to use MOCK to learn dynamical systems. This method scales linearly with the number of dimensions of the state space. Building upon Rosenfeld et al. (2019a;b); Russo et al. (2021), we provide a derivation with the help of vector-valued Reproducing Kernel Hilbert spaces (vvRKHSs) which allows for a reduction in computational complexity in special cases and extensions to physics informed kernels. We also emphasize the simplicity of the algorithm and demonstrate competitive performance on high-dimensional data, as well as noisy data. Finally, in section 5 we craft a vvRKHS for learning divergence-free vector fields, demonstrating the versatility of the MOCK method.

Rosenfeld and Russo extend the setting of ridge regression to the case of learning a vector field using snapshots of trajectories, as presented in the paper Rosenfeld et al. (2019a) and the follow-up paper Rosenfeld et al. (2024). In both papers, a finite basis set of vector-valued functions was used to learn the unknown slope field. The provided solution is equivalent to optimizing in a vvRKHS with an explicit kernel. Using an I-separable kernel, we allow our parameter count to increase linearly with the state space dimension (d) while maintaining computational complexity that increases only linearly in d . In contrast, the model proposed by Rosenfeld and Russo requires computational complexity to increase cubically with the number of parameters of the learned model.

In addition, we generalize this work to arbitrary matrix-valued kernels. Note that we keep the least square setting of ridge regression while in Rosenfeld et al. (2024), Rosenfeld and Russo used a more general weak formulation with Liouville operators. We create a benchmark and compare MOCK against the state-of-the-art algorithms. We also benchmark several kernels, including Gaussian, Laplace, Matérn, and random Fourier features. Lastly, in section 5, we present an application where the vvRKHS is made of divergence-free kernels. Using simulated data, we present an experiment in which the use of a divergence-free kernel improved the recovery of the vector field compared to an ordinary kernel.

Without any restriction on the vvRKHS, learning a vector field with MOCK requires solving an (Nd, Nd) system, where N is the total number of snapshots and d is the dimension of the state space. Improvements can be obtained when the kernel is a tensor product of univariate kernels. In this case, one needs to solve d (N, N) linear systems. When the univariate kernel is explicit, one can instead solve d (q, q) linear systems. By contrast, Russo and Rosenfeld considered a loss equivalent to the case of an arbitrary explicit vvRKHS without the Kronecker product structure. This has the drawback of requiring a runtime that scales cubically with the total number of parameters in the model (requires solving a $dq \times dq$ linear system). This is also shared by SINDy and the explicit forms of DMD.

2 Background

2.1 vvRKHS for modeling vector fields

Scalar RKHSs are spaces of real-valued functions made popular for their use in constructing the kernelized support vector machine classifier Schölkopf & Smola (2002) chapter III. Scalar RKHSs generalize to vvRKHSs and provide simple nonparametric models for vector fields. A matrix-valued kernel fully characterizes a vvRKHS. The choice of this kernel is left to the user and allows for encoding various properties of the functions in the corresponding vvRKHS. Choosing a kernel with Lipschitz continuous diagonal elements guarantees that all functions in the vvRKHS \mathbb{H} are Lipschitz continuous. This, in turn, guarantees the local existence and uniqueness of the solutions to the associated ordinary differential equation $\dot{x} = f(x)$ where

$f \in \mathbb{H}$, see Lahouel et al. (2022). Furthermore, one may allow the inclusion of physics-inspired constraints into the function space by appropriately choosing the kernel, and an example of a divergence-free vvRKHS is provided in section 5. Kernels come in two forms: implicit and explicit. The former implicitly characterizes a mapping from \mathbb{R}^d to a Hilbert space, which can be of infinite dimension. Examples include the family of Matérn kernels, which contain the familiar Gaussian and Laplace kernels. The latter explicitly characterizes a mapping from \mathbb{R}^d to \mathbb{R}^p for some p . Examples include polynomial kernels and random Fourier features. Both kernel types will be used in the experiments in section 4. We now provide a mathematical presentation of kernels and vvRKHSs.

2.2 Vector-Valued RKHS (vvRKHSs)

Definition 1. Let $\mathcal{M}_{(d,d)}$ be the set of (d,d) matrices, $d \geq 1$. A positive definite matrix-valued kernel K is a mapping: $\mathcal{X} \times \mathcal{X} \mapsto \mathcal{M}_{(d,d)}$, such that

1. symmetric: $K(x, x') = K(x', x)^T$, for any $x, x' \in \mathcal{X}$; M^T denotes the transpose of the matrix M .
2. positive definite: for any x_1, \dots, x_n in \mathcal{X} , and for any w_1, \dots, w_n in \mathbb{R}^d ,

$$\sum_{i,j} w_i^T K(x_i, x_j) w_j \geq 0 \quad (1)$$

The simplest kernels are the *separable* kernels

$$K(x, x') = k(x, x') A \quad (2)$$

where k is a positive definite scalar kernel and A is a positive semi-definite (PSD) matrix. When $A = I$, \mathbb{H} is made of d copies of the RKHS of k . We call such a kernel I-separable. If the kernel $k(x, x')$ is an explicit kernel (can be written as $\phi(x)^T \phi(x')$ for some function $\phi: \mathbb{R}^d \rightarrow \mathbb{R}^q$) it has the additional properties:

$$K(x, x') = \phi(x)^T \phi(x') I \quad (3)$$

$$= (\phi(x)^T \phi(x')) \otimes (I^T I) \quad (4)$$

$$= (\phi(x) \otimes I)^T (\phi(x') \otimes I) \quad (5)$$

where \otimes denotes the Kronecker product. Defining $\Psi(x) : \mathbb{R}^d \rightarrow \mathbb{R}^{qd \times d}$ by

$$\Psi(x) = \phi(x) \otimes I, \quad (6)$$

we see that the matrix-valued explicit kernel is

$$K(x, x') = \Psi(x)^T \Psi(x') \quad (7)$$

All kernels used in our experiments in section 4 are of the I-separable form, while the divergence-free kernel in section 5 is not an I-separable kernel. There are three ways to characterize a vvRKHS. They are presented in appendix D for completeness. Here, we briefly present the construction using the Riesz representation theorem, which is critical in developing the MOCK algorithm.

Definition 2. Let \mathbb{H} be a Hilbert space of functions $\mathcal{X} \rightarrow \mathbb{R}^d$. We denote by $\langle \cdot, \cdot \rangle$ the inner product in \mathbb{H} and $\|\cdot\|_{\mathbb{H}}$ or simply $\|\cdot\|$ the associated norm. Critically, we assume that for any $x \in \mathcal{X}$, the evaluation functional $f \mapsto f(x)$ is continuous, that is, there is a constant $M_x \in \mathbb{R}$, such that

$$\|f(x)\|_{\mathbb{R}^d} \leq M_x \|f\|_{\mathbb{H}} \quad (8)$$

for all $f \in \mathbb{H}$. Then, using the Riesz representation theorem, for any direction $v \in \mathbb{R}^d$, there exists a unique function in \mathbb{H} denoted $\phi_{x,v}^*$ such that

$$v^T f(x) = \langle f, \phi_{x,v}^* \rangle \quad (9)$$

Define the matrix-valued kernel K such that

$$K_{ij}(x, x') = \langle \phi_{x, e_i}^*, \phi_{x', e_j}^* \rangle, i, j = 1 \dots d \quad (10)$$

where e_1, \dots, e_d is the natural basis of \mathbb{R}^d . Then K is a kernel, \mathbb{H} is the vvRKHS of K and $\phi_{x, v}^*(\cdot) = K(\cdot, x)v$. The reproducing property of the kernel is, for any $f \in \mathbb{H}$, $x \in \mathcal{X}$, and $v \in \mathbb{R}^d$,

$$v^T f(x) = \langle f, K(\cdot, x)v \rangle \quad (11)$$

2.3 Occupation kernel functions for vvRKHS

The notion of occupation kernel functions, introduced in Rosenfeld et al. (2019a), is central to this work. Let \mathbb{H} be a vvRKHS of functions $\mathbb{R}^d \rightarrow \mathbb{R}^d$ with kernel K . Consider a parametric curve $x: [a, b] \rightarrow \mathbb{R}^d$, $t \mapsto x(t)$ and define the operator L_x from \mathbb{H} to \mathbb{R}^d , $L_x(f) = \int_a^b f(x(t))dt$. L_x is linear. If $x \mapsto K_{ii}(x, x)$ is continuous for each $i = 1 \dots d$, then L_x is also continuous¹. For each $v \in \mathbb{R}^d$, the occupation kernel function of the curve x in the direction v , denoted $L_{x, v}^*$, is then defined as the element in \mathbb{H} such that $v^T L_x(f) = \langle f, L_{x, v}^* \rangle$ for all $f \in \mathbb{H}$. By the Riesz representation theorem, this element exists and is unique.

Let us now provide a useful characterization of $L_{x, v}^*$ in terms of the curve x , the vector v and the kernel matrix K . Note that for any $w \in \mathbb{R}^d$

$$\begin{aligned} w^T L_{x, v}^*(y) &= \langle L_{x, v}^*, K(\cdot, y)w \rangle \\ &= \langle K(\cdot, y)w, L_{x, v}^* \rangle \\ &= v^T L_x(K(\cdot, y)w) \\ &= v^T \int_a^b K(x(t), y)w dt \\ &= w^T \left[\int_a^b K(y, x(t))dt \right] v \end{aligned} \quad (12)$$

thus

$$L_{x, v}^*(\cdot) = \left[\int_a^b K(\cdot, x(t))dt \right] v \quad (13)$$

Here, we used the reproducing property equation 11, the symmetry of the inner product, the definition of the occupation kernel and the functional L_x , and the symmetry of the kernel K . It is convenient to notate the matrix of functions

$$M_x(\cdot) = \int_a^b K(\cdot, x(t))dt \quad (14)$$

so that the $L_{x, v}^*(\cdot) = M_x(\cdot)v$. When K is an I-separable kernel, this reduces to $L_{x, v}^*(\cdot) = \left(\int_a^b k(\cdot, x(t))dt \right) v$

Using the same arguments (see appendix D.2), we find

$$\langle L_{x, v}^*, L_{y, w}^* \rangle = v^T \left[\int_a^b \int_a^b K(x(s), y(t))dsdt \right] w \quad (15)$$

It is also convenient to use the notation

$$M_{x, y} = \int_a^b \int_a^b K(x(s), y(t))dsdt \quad (16)$$

¹A derivation is provided in appendix D.1

so that

$$\langle L_{x,v}^*, L_{y,w}^* \rangle = v^T M_{x,y} w. \quad (17)$$

Note that when K is I-separable,

$$\langle L_{x,v}^*, L_{y,w}^* \rangle = \left(\int_a^b \int_a^b k(x(s), y(t)) ds dt \right) v^T w. \quad (18)$$

3 Methods

Consider the ODE

$$\dot{x} = f_0(x), x \in \mathbb{R}^d \quad (19)$$

where $f_0 : \mathbb{R}^d \rightarrow \mathbb{R}^d$ is a fixed, unknown vector field. Consider also n curves

$$x_1(t), \dots, x_n(t), [a_i, b_i] \rightarrow \mathbb{R}^d, i \in \{1, \dots, n\} \quad (20)$$

3.1 The multivariate occupation kernel (MOCK) algorithm

We describe the MOCK algorithm in two steps. In the first step, we assume that we observe the curves in equation 20. We aim to recover the vector field f_0 driving the ODE in equation 19. Assuming that this vector field belongs to a vvRKHS, and under a penalized least square loss, we provide a solution expressed in terms of occupation kernel functions. In the second step, we relax the hypothesis and assume that snapshots along these trajectories are provided in place of the trajectories. Rearranging these trajectories and replacing the integrals with numerical quadratures makes the problem tractable.

3.2 The occupation kernel algorithm from curves

Let us design an optimization setting, an inverse problem, for recovering f_0 from these trajectories. Let \mathbb{H} be a vvRKHS of continuous vector-valued functions $\mathbb{R}^d \rightarrow \mathbb{R}^d$, $\lambda > 0$ a constant, and let us define the functional,

$$J(f) = \frac{1}{n} \sum_{i=1}^n \left\| \int_{a_i}^{b_i} f(x_i(t)) dt - x_i(b_i) + x_i(a_i) \right\|_{\mathbb{R}^d}^2 + \lambda \|f\|_{\mathbb{H}}^2 \quad (21)$$

The first term is minimized when $f = f_0$. This is a consequence of the fundamental theorem of calculus. However, aside from degenerate cases, this minimizer is not unique. Thus, the second term is a regularization term. The problem of minimizing equation 21 over \mathbb{H} is well-posed. It has a unique solution that can be expressed using the occupation kernel functions as follows:

Theorem 1. *The unique minimizer of J over the vvRKHS \mathbb{H} with kernel K is*

$$f^*(\cdot) = \sum_{i=1}^n L_{x_i, \alpha_i}^*(\cdot) = \sum_{i=1}^n M_{x_i}(\cdot) \alpha_i, \alpha_i \in \mathbb{R}^d \quad (22)$$

where L_{x_i, α_i}^* is the occupation kernel function of the curve x_i along the interval $[a_i, b_i]$ in the direction α_i , that is

$$L_{x_i, \alpha_i}^*(\cdot) = \left[\int_{a_i}^{b_i} K(\cdot, x_i(t)) dt \right] \alpha_i = M_{x_i}(\cdot) \alpha_i \quad (23)$$

and where the vector $\alpha = (\alpha_1^T, \dots, \alpha_n^T)^T$ is the solution of

$$\begin{aligned} (M + \lambda n I) \alpha &= x(b) - x(a), \\ x(a) &= (x_1(a_1)^T, \dots, x_n(a_n)^T)^T, \\ x(b) &= (x_1(b_1)^T, \dots, x_n(b_n)^T)^T \end{aligned} \quad (24)$$

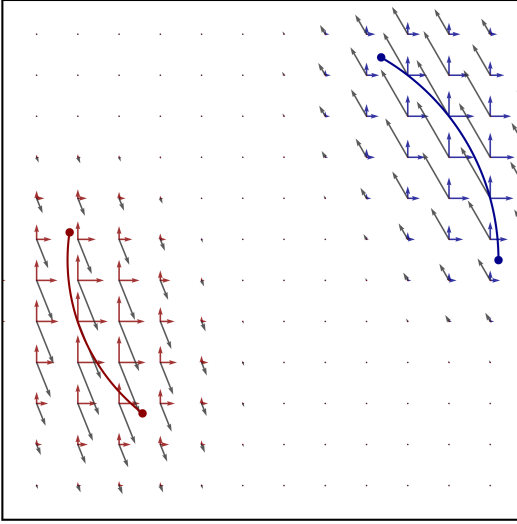


Figure 1: Illustration of the MOCK algorithm with the Gaussian separable kernel. We observe the red and blue trajectories, respectively \mathbf{x}_1 and \mathbf{x}_2 (running counterclockwise). The horizontal and vertical red vector fields correspond respectively to the occupation kernel functions $L_{\mathbf{x}_1, e_1}^*$ and $L_{\mathbf{x}_1, e_2}^*$ and similarly for the horizontal and vertical blue vector fields \mathbf{x}_2 . The influence of each trajectory is local. The grey vector field is the MOCK algorithm solution, a linear combination of the red and blue vector fields.

and M is the (nd, nd) matrix made of (d, d) blocks, each defined by

$$M_{ij} = M_{x_i, x_j} = \int_{t=a_j}^{b_j} \int_{s=a_i}^{b_i} K(x_i(s), x_j(t)) ds dt \quad (25)$$

To build some intuition about how the ridge penalty term ensures well-posedness of the minimization problem, suppose that many vector fields can generate trajectories perfectly fitting the data, making the first term in the cost function equal to zero. Occam's razor dictates choosing the simplest such vector field. Here, simplicity corresponds to the smallest vvRKHS norm as measured by the second term. The strict convexity of the squared vvRKHS norm ensures that no two solutions can have the same minimal norm. Indeed, any convex combination of such solutions would yield a smaller norm, contradicting the minimality assumption. Therefore, the minimizer is unique.

The proof of theorem 1 is a natural generalization of the representer theorem in RKHSs. It is presented in appendix E. Figure 1 illustrates the result of the theorem. In the case of an implicit I-separable kernel, the linear system in equation 24 decouples into d linear systems, each of size $n \times n$ where n is the number of trajectories. This allows for an algorithm linear in d . If the I-separable kernel derives from an explicit scalar-valued kernel, the linear systems are $q \times q$ where q is the number of dimensions of the scalar-valued kernel. The experiments in section 4 exploit this remarkable situation. The experiments in section 5 use non-separable kernels. This is a tractable design when d is not too large.

3.3 The occupation kernel algorithm from data

Let us now assume that instead of observing n curves that are solutions of equation 19, we observe $m + 1$ snapshots, sometimes noisy, $z_i = (z_i^{(0)}, \dots, z_i^{(m)})$ at time-points t_0, \dots, t_m coming from a true trajectory x_i , $i = 1 \dots n$. Firstly, we reshape this data into observations coming from $N = mn$ trajectories, each made of

two samples. This is done by viewing every couple of consecutive observations as two observations associated with a single trajectory. In other words, we assume that we observe (possibly with noise) the initial and final points of N trajectories $x_i, i = 1 \dots N$, that we denote by $z_i = (z_i^{(0)}, z_i^{(1)})$, the times at which $z_i^{(0)}$ and $z_i^{(1)}$ are sampled are denoted by $t_i^{(0)}$ and $t_i^{(1)}$. z_i is a matrix of dimensions d by 2.

Secondly, we replace the integral in equation 23 by an integral quadrature, noted \oint , and the double integral in equation 25 by a double integral quadrature, noted $\oint\oint$. Observations z_i are used to compute the quadrature involving the trajectory x_i . In both cases, we use the trapezoidal rule, providing

$$\oint K(\cdot, x_i(t)) dt = \frac{(t_i^{(1)} - t_i^{(0)})}{2} \left(K(\cdot, z_i^{(0)}) + K(\cdot, z_i^{(1)}) \right) \quad (26)$$

and

$$\begin{aligned} \oint\oint K(x_i(s), x_j(t)) ds dt &= \frac{(t_i^{(1)} - t_i^{(0)})(t_j^{(1)} - t_j^{(0)})}{4} \left(K(z_i^{(0)}, z_j^{(0)}) + K(z_i^{(0)}, z_j^{(1)}) \right. \\ &\quad \left. + K(z_i^{(1)}, z_j^{(0)}) + K(z_i^{(1)}, z_j^{(1)}) \right) \end{aligned} \quad (27)$$

The resulting algorithms for learning the vector field and predicting a trajectory given an initial condition are presented in Alg. 1 and Alg. 2 respectively. Alg. 1 and Alg. 2 are simplified and do not contain the optimizations implemented to reduce the computational complexity (see section 3.4). The linear system in line 5: of Algorithm 1 is solved using `numpy.linalg.solve` from NumPy v1.26.4

Algorithm 1 MOCK learning: Estimate the parameters defining the vector field.

Require: Training data. $z_i, i = 1 \dots N$ (N matrices of dimension $(d, 2)$)

- 1: Compute $\delta = (z_1^{(1)} - z_1^{(0)}, \dots, z_N^{(1)} - z_N^{(0)})^T \in \mathbb{R}^{N \times d}$
- 2: **for** $i = 1 \dots N, j = 1 \dots N$ **do**
- 3: $M_{ij} \leftarrow \oint\oint K(x_i(s), x_j(t)) ds dt$
- 4: **end for**
- 5: Solve the linear system $(M + \lambda NI) \alpha = \delta$ for α
- 6: **Return:** α

Algorithm 2 MOCK inference: Generate trajectories given initial conditions.

Require: Training data. $z_i, i = 1 \dots N$. (N matrices of dimension $(d, 2)$)

Require: Output of algorithm 1: $\alpha = (\alpha_1, \dots, \alpha_n)^T$.

Require: Initial conditions. p vectors : (y_1^0, \dots, y_p^0)

- 1: **for** $j = 1 \dots p$ **do**
- 2: Using a numerical integrator, generate the solution of:

$$\begin{cases} \dot{y}_j = f^*(y_j) \\ y_j(0) = y_j^0 \end{cases}$$

- 3: $f^*(y_j) = \sum_{i=1}^N [\oint K(y_j, x_i(t)) dt] \alpha_i$
- 4: **end for**

3.4 Computational complexity

We specialize to the separable kernels case with $A = I$, see section 2.2. In such a case, the linear system in equation 24 becomes equivalent to solving an $N \times N$ linear system where the right-hand side is $N \times d$. Therefore, this requires $O(dN^2)$ to construct the kernel matrix, $O(N^2)$ to estimate the integrals, and

$O(dN^3)$ to solve the linear system. Overall, the MOCK algorithm is thus linear in d . The space complexity is $O(N^2)$.

On the other hand, if we let $\psi(x) \in \mathbb{R}^{d \times q}$, then $K(x, y) = \psi(x)^T \psi(y) \in \mathbb{R}^{d \times d}$ is an explicit kernel. In such a case, a $q \times q$ linear system is solved to find f , requiring $N, d \times q$ by $q \times d$ matrix-matrix multiplications to construct the system. This provides a computational complexity of $O(dNq^2 + q^3)$. Further details are provided in appendix F.

4 Experiments

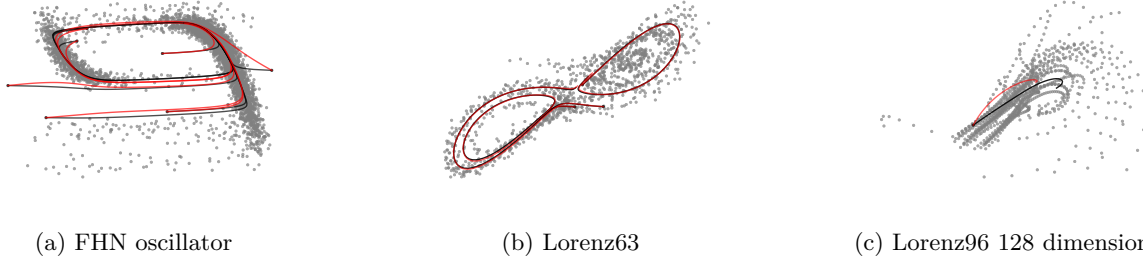


Figure 2: The grey points are the training data. The black curves are the test trajectories. The red curves are the predictions on the test set. For data in dimensions higher than two, only the first two dimensions are shown.

4.1 Datasets

We test the methods on a diverse set of synthetic and real-world datasets that reflect the challenges of learning systems of ODEs. Table 1 provides the dimension of the state space, the number of trajectories, and the average number of snapshots per trajectory for each of the 9 datasets considered. In each data set, the trajectories were partitioned into training (60%), validation (20%), and testing (20%) sets.

Name	Type	d	n	m
NFHN	Synthetic	2	150	201
Lorenz63	Synthetic	3	150	201
Lorenz96-16	Synthetic	16	100	243
Lorenz96-32	Synthetic	32	100	243
Lorenz96-128	Synthetic	128	100	243
Lorenz96-1024	Synthetic	1024	100	100
CMU	Real	50	75	106.7
Plasma	Real	6	425	2.95
Imaging	Real	117	231	2.26

Table 1: For each dataset, d is the number of dimensions of the system, which is the dimension of the state-space, n is the total number of trajectories, and m is the average number of samples per trajectory. In each data set, the trajectories were partitioned into training (60%), validation (20%), and testing (20%) sets.

Noisy FitzHugh-Nagumo (NFHN) The FitzHugh-Nagumo oscillator FitzHugh (1961) is a nonlinear 2D dynamical system that models the basic behavior of excitable cells, such as neurons and cardiac cells². We add considerable noise to this otherwise simple dataset (see figure 3).

Noisy Lorenz63 (Lorenz63) The Lorenz63 system Lorenz (1963) is a 3D system provided as a simplified model of atmospheric convection.

²Further details of the all datasets are provided in appendix B.

Lorenz96 The Lorenz96 data arises from Lorenz (1995) in which a system of equations is proposed that may be chosen to have any dimension greater than 3. (Lorenz96-16) has 16 dimensions, etc.

CMU Walking (CMU) The Carnegie Mellon University (CMU) Walking data is a repository of publicly available data. It can be found at <http://mocap.cs.cmu.edu/>.

Plasma This dataset includes imaging and plasma biomarkers from the WRAP study, see Johnson et al. (2018).

Imaging This dataset includes regional imaging biomarkers from the WRAP study, see Johnson et al. (2018).

4.2 Data format

Each dataset is stored as a rectangular matrix. Each row corresponds to a data point. The columns include the id of the trajectory, the time, the features, and three binary columns indicating whether the row is to be used for training, validation, or testing.

4.3 Kernels, regularization, and hyperparameter tuning for the MOCK algorithm

We train the MOCK models using the scalar-valued Matérn kernels, including the Gaussian, Laplace, and C^{10} kernels Fuselier et al. (2016). The analytic expressions are provided in Appendix C.2. We also train an explicit kernel with 200 Fourier Random features Rahimi & Recht (2007). We use Bayesian optimization for hyperparameter tuning of the regularization parameter λ and bandwidth parameter σ . λ controls the smoothness of the solution, while σ controls the relevant scale for the input data. Specifically, we use the `gp_minimize` function from the Scikit-Optimize (`skopt`) package, **version 0.10.2**, which implements Gaussian Process optimization.

4.4 Comparable methods

We select competitive methods covering various categories.

Sparse Identification of Nonlinear Dynamics (SINDy) SINDy is a well-developed class of data-driven methods for identifying dynamical systems models from trajectories. Brunton et al. (2016) These methods rely on sparse regression techniques to isolate the most relevant terms in the governing equations from a set of candidate functions. SINDy demonstrates robustness for sparse and limited data Kaheman et al. (2020); Fasel et al. (2022).

Reduced Order Models (ROMs) ROMs are a class of methods for simplifying high-dimensional dynamical systems by projecting them onto a lower-dimensional space. Dynamic mode decomposition (DMD) is a data-driven method for extracting spatiotemporal patterns and coherent structures from high-dimensional data generated by dynamical systems Tu (2013). eDMD extends DMD to handle nonlinear dynamics by working in a higher-dimensional feature space. Williams et al. (2015). We benchmark with eDMD-RFF Lew et al. (2023), eDMD-Poly Williams et al. (2015), and eDMD-Deep Yeung et al. (2019)

Deep Learning Methods Deep learning methods can be used in conjunction with ROMs to learn transformations to lower-dimensional spaces. These methods use deep learning to construct an efficient representation of the dynamical system and to capture nonlinear dynamics Lusch et al. (2018); Yeung et al. (2019); Li et al. (2019). Deep learning methods can also be incorporated into the SINDy framework to identify sparse, interpretable, and predictive models from data Champion et al. (2019); Bakarji et al. (2022). We benchmark with ResNet He et al. (2016) Lu et al. (2021)

Latent ODEs for Irregularly-Sampled Time Series The Latent ODE method (also a deep learning method Rubanova et al. (2019)) is an update of the Neural ODEs model introduced in Chen et al. (2018). The core idea is to represent the hidden dynamics of time series data in a continuous latent space using ODEs. Given the latent trajectory, the observations of the time series are assumed to be independent. The latent trajectory dynamics are governed by a neural ODE model. The model uses an encoder-decoder framework

where the encoder maps observed data to a latent initial value via an RNN architecture. The hidden states are then carried through neural ODEs between times of observations. Finally, the decoder generates the latent trajectory forward in time and predicts future observations.³

The hyperparameters for each method are shown in Table 4 in appendix G. All experiments are run in Google Colab using the default settings. The GPU was only enabled (A100, High-RAM) for the deep learning techniques. Lastly, to get an idea of the difficulty of each problem, we compare all methods against the null model, which predicts no change, that is $x(t) = x_0$ for all $t \in [a, b]$. Datasets for which no models are able to do much better than this null model are difficult datasets to learn and perhaps less useful for benchmarking learning methods.

4.5 Evaluation Method

For each dataset, the trajectories were partitioned into training, validation, and testing. At test time, we integrated the predicted trajectories starting at the given initial conditions and compared to the true trajectories. To measure the performance of each method, we define two types of errors for each trajectory of the test set. We define:

$$\text{Err} = \sqrt{\sum_{i=2}^m (t_i - t_{i-1}) \|y_i - \hat{y}_i\|^2} \quad (28)$$

where y_i and \hat{y}_i are the observed and predicted trajectory samples at time t_i , respectively. Additionally, we define 1-Err by setting $m = 2$ in equation 28. All the methods were trained, validated, and tested on the same data. Table 2 provides the average Err and 1-Err errors across the trajectories of the test set. To test whether the MOCK methods are (statistically) significantly better than comparable methods and vice versa, we first generated a Wilcoxon test p-value for every MOCK method (four different kernels) against the other comparable methods. The pairs of observations used in the test are the errors of the two compared methods for every trajectory in the test set. Finally, to generate a p-value comparing all MOCK methods together against another comparable method, we used Fisher’s method Mosteller & Fisher (1948) to combine the four p-values of the MOCK methods. We report a * in Table 2 if the group of MOCK methods is significantly better ($p < 0.01$) and † if the compared method outperforms MOCK with statistical significance ($p < 0.01$). Otherwise, no method is significantly better than the other.

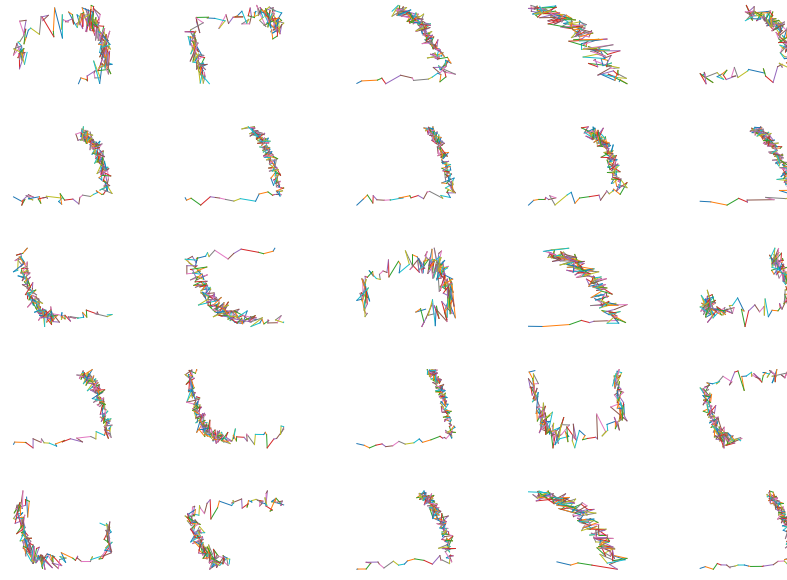
4.6 Evaluation Performance

Examples of the output of the MOCK algorithm are presented visually in figures 2 and 4. Table 2 summarizes the prediction errors for each experiment. While no single method outperforms other methods over all datasets, MOCK outperforms all other methods in 3 of the 9 datasets (on the task of full trajectory prediction, denoted Err), and outperforms all other methods on 4 of the 9 datasets on the task of predicting the next sample (denoted 1-Err). It also performs competitively on the remaining datasets on both tasks. Notably, eDMD-Deep yielded the best results for the CMU experiments. Deep learning models and DMD methods learn the dynamics in a feature space and therefore have less stringent constraints on the dynamics. We believe this is why they outperform with datasets such as the CMU dataset as our model assumes the dynamics arises from a homogeneous system, and this is not the case with the CMU dataset. See Appendix B.2.

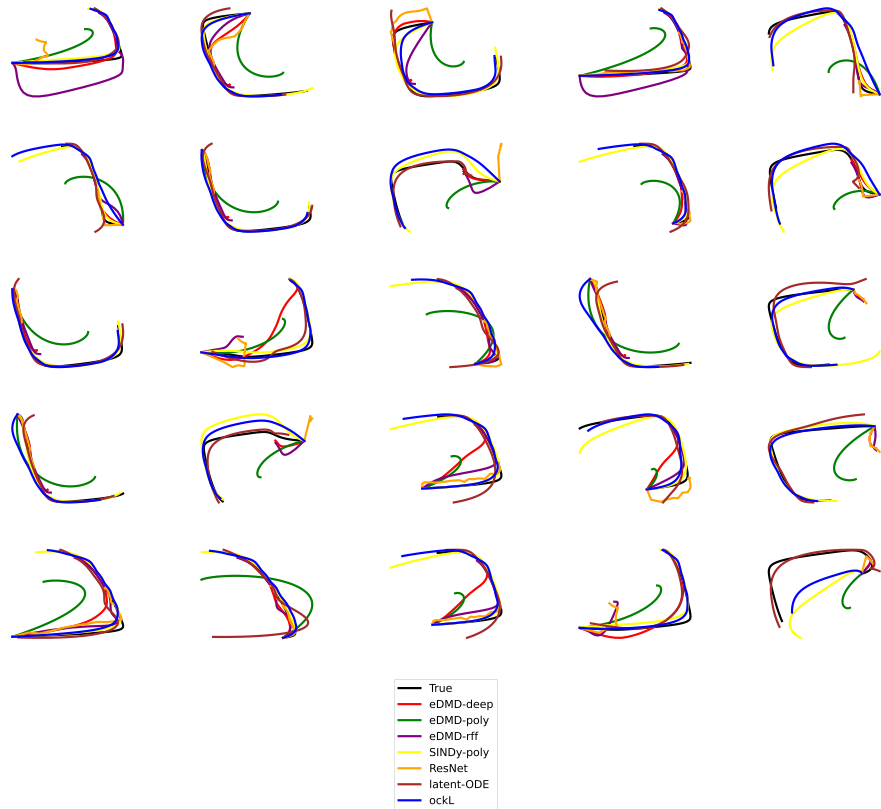
The differences observed in table 2 are not always significant. Recall that we use the sign † when a method is better than all the MOCK methods. We count 5 models out of 9 with at least one † for Err and only 2 out of 9 for the 1-Err. Note that the MOCK algorithm is optimized for the 1-Err since the trajectories of the training set are systematically reshaped into trajectories of two observations. Thus it is not surprising that it performs better for this metric.

When comparing the kernels used for the MOCK method, the Laplace kernel performs the best overall, consistent with other analyses of this kernel (Geifman et al. (2020)). Note also that the random Fourier

³Latent ODEs was implemented using the Github repository: https://github.com/YuliaRubanova/latent_ode. The subsampling was disabled for the Plasma and Imaging datasets because the training trajectories were too short in these datasets.



(a) 25 randomly sampled trajectories in the NFHN (Noisy FHN) training set.



(b) 25 randomly sampled trajectories in the test set for NFHN. Black: true trajectory, red: eDMD-deep, green: eDMD-poly, purple: eDMD-rff, yellow: SINDy-poly, orange: ResNet, brown:latent-ODE, and blue:ockL.

Figure 3: NFHN dataset

Table 2: Dynamical System Estimation Results

Lorenz63			NFHN			Lorenz96-16		
	Err	1-Err		Err	1-Err		Err	1-Err
ResNet	2.07*	.014*	ResNet	5.94*	.064*	ResNet	6.42*	.010*
eDMD-Deep	2.91*	.009*	eDMD-Deep	4.54*	.036*	eDMD-Deep	5.93*	.040*
eDMD-Poly	2.22*	.012*	eDMD-Poly	4.10*	.037*	eDMD-Poly	6.91*	.036*
eDMD-RFF	1.93*	.011*	eDMD-RFF	4.01*	.037*	eDMD-RFF	6.22*	.029*
null	2.56*	.011*	null	9.69*	.043*	null	7.50*	.039*
SINDy-Poly	.99*	.002	SINDy-Poly	1.68*	.022[†]	SINDy-Poly	.40*	.0003*
ockG	.66	.002	ockG	1.40	.029	ockG	.69	.0007
ockL	.65	.002	ockL	1.11	.030	ockL	.22	.0001
ockM	2.52	.012	ockM	1.41	.029	ockM	.22	.0001
ockF	2.52	.012	ockF	1.38	.028	ockF	.22	.0001
Lode	1.49*	.092*	Lode	.64[†]	.131*	Lode	3.82*	.138*
Lorenz96-32			Lorenz96-128			Lorenz96 -1024		
	Err	1-Err		Err	1-Err		Err	1-Err
ResNet	11.56*	.020*	ResNet	24*	2.64*	ResNet	66.1*	6.48*
eDMD-Deep	8.79*	.057*	eDMD-Deep	17*	.089*	eDMD-Deep	26.9*	.41*
eDMD-Poly	9.67*	.051*	eDMD-Poly	19*	.109*	eDMD-Poly	61.5*	.42*
eDMD-RFF	8.10*	.028*	eDMD-RFF	16 [†]	.201*	eDMD-RFF	54.2*	.38*
null	10.49*	.056*	null	21*	.112*	null	67.0*	.16*
SINDy-Poly	8.56*	.037*	SINDy-Poly	19*	.066*	SINDy-Poly ^{**}	NA	NA
ockG	.47	.0001	ockG	17	.064	ockG	18.0	.013
ockL	.48	.0001	ockL	16	.035	ockL	17.8	.014
ockM	.49	.0001	ockM	16	.040	ockM	17.9	.013
ockF	.47	.0001	ockF	16	.036	ockF	18.0	.015
Lode	6.06*	.217*	Lode	15[†]	.342*	Lode	15.8[†]	1.04*
Plasma			Imaging			CMU		
	Err	1-Err		Err	1-Err		Err	1-Err
ResNet	4.93*	2.89*	ResNet	27.4*	19.4*	ResNet	22.6*	.86 [†]
eDMD-Deep	4.09	2.42	eDMD-Deep	15.6*	12.5	eDMD-Deep	15.7 [†]	2.03*
eDMD-Poly	4.01	2.39	eDMD-Poly	15.7	12.5	eDMD-Poly	14.9[†]	.78 [†]
eDMD-RFF	4.07	2.43	eDMD-RFF	27.9*	19.3*	eDMD-RFF	14.9 [†]	.76[†]
null	4.00*	2.41	null	16.2*	12.6*	null	21.6*	1.01*
SINDy-Poly	3.95	2.40	SINDy-Poly	96.1*	53.7*	SINDy-Poly	33.8*	.91*
ockG	3.96	2.41	ockG	15.6	12.3	ockG	21	.89
ockL	3.96	2.41	ockL	15.6	12.3	ockL	19.6	.93
ockM	3.96	2.41	ockM	15.7	12.3	ockM	21.5	1.01
ockF	3.96	2.41	ockF	15.8	12.4	ockF	21.6	1.01
Lode	4.28*	2.68*	Lode	14.8[†]	11.7	Lode	14.9 [†]	1.88*

Description: Minimum values are in bold. A * indicates a significant (Fisher's method) p-value (< 0.01) in favor of the ock methods in the comparison. A [†] indicates a significant p-value in favor of the method compared with all ock methods. There is no statistically significant difference otherwise. Our models are labelled as ockG - occupation kernel method with Gaussian kernel, ockM - occupation kernel method with Matérn kernel, ockF - occupation kernel method with Random Fourier Features (RFF), and ockL - occupation kernel with Laplace kernel (See section 4.2). We compare against SINDy-Poly, eDMD-Deep, eDMD-Poly, eDMD-RFF, ResNet and Latent Ode (Lode) (See section 4.3). ^{**} No result could be obtained for SINDy-Poly for this dataset due to computational complexity issues.

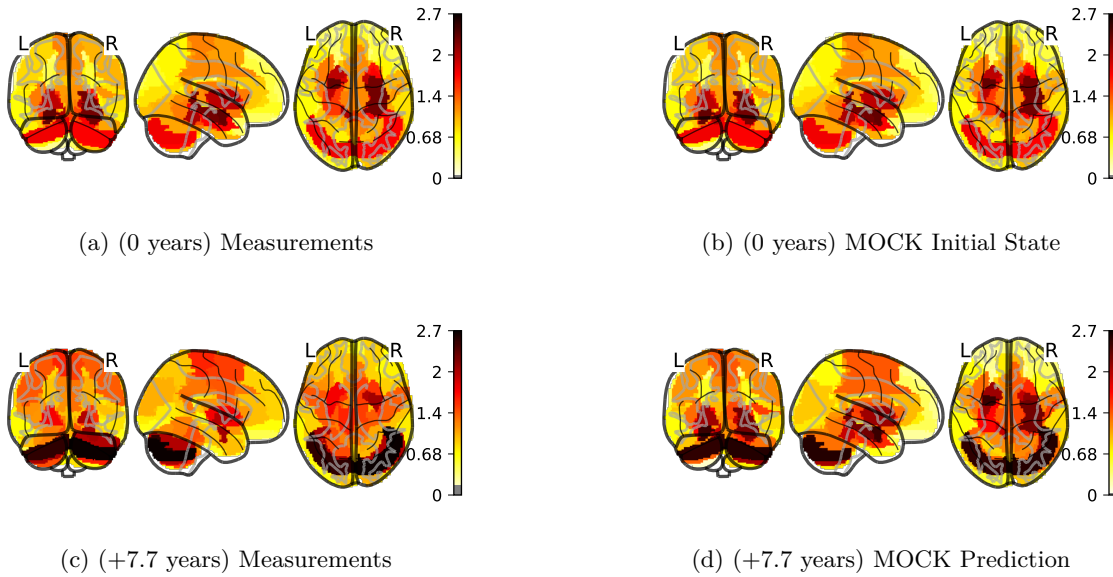


Figure 4: MOCK Predicted Biomarker Values from the imaging dataset.

features kernel, which approximates the Gaussian kernel, performs well for all datasets, allowing for linear implementations in N , which is the number of examples in the training set. Moreover, we use the same number of features (200) in all cases, leading to models with parameter sizes of $200 \cdot d$ for Fourier random feature implementations. Importantly, because our model size scales linearly with d we do not need to increase the number of Fourier random features for higher dimensional problems.

The trajectories predicted by ockL for NFHN (in blue in figure 3b) are visually close to the ground truth (in black) in all but the last case. SINDy-poly (in yellow) is competitive. ResNet provides very irregular trajectories. Latent ODE provides good long-term predictions. However, the initial points do not coincide with the initial points of the ground truth provided for all the algorithms. In other words, while Latent-ODE performs very well on the task of predicting full trajectories, it performs very poorly on the next sample prediction task which is an inherent limitation of some deep learning models like Latent-ODE and Resnet.

We tested MOCK with a dataset of 1024 dimensions to show how well it scales. The implementation of SINDy-Poly that we used did not provide a result for this data due to runtime issues; see NA in the table 2.

4.7 Comparative computational complexity

The computational complexities are compared in table 3. The MOCK algorithm with implicit and explicit kernel is linear in d , the dimension of the state space. Resnet and Lode are quadratic in d . In principle, SINDy-Poly, eDMD-Poly, eDMD-RFF, and eDMD-Deep are linear in d . However, q , the number of parameters in the learned model, needs to increase with d to obtain acceptable performances. This means the complexity is, in practice, more than linear in d . In the case of SINDy-Poly with quadratic basis functions, q is $\mathcal{O}(d^2)$.

5 Learning vector fields with constraints

Divergence-free ($\nabla \cdot v = 0$) and curl-free ($\nabla \times v = 0$) vector fields appear in a diverse set of applications including fluid dynamics Wendland (2009); Fuselier et al. (2016), magnetohydrodynamics McNally (2011) and modeling magnetic fields Wahlström et al. (2013), image processing Polthier & Preuß (2003), and surface reconstruction Drake et al. (2022). Accordingly, a significant amount of research has been devoted to the development of curl-free and divergence-free kernel methods Narcowich & Ward (1994); Lowitzsch (2005); Narcowich et al. (2007); Fuselier (2008); Fuselier & Wright (2009); Gao et al. (2022); Scheuerer &

MOCK implicit	MOCK explicit	ResNet	eDMD-Deep
$\mathcal{O}(dN^3)$	$\mathcal{O}(dNq^2 + dq^3)$	$\mathcal{O}(kd^2TN)$	$\mathcal{O}(TN(Ldq + q^2) + dq^2 + q^3)$
eDMD-Poly	eDMD-RFF	Lode	SINDy-Poly
$\mathcal{O}((N+d)q^2 + N^2q + q^3)$	$\mathcal{O}((N+d)q^2 + q^3)$	$\mathcal{O}(nT(k_1d^2 + k_2q^2))$	$\mathcal{O}(T(qd + q^3 + dNq^2))$

Table 3: Runtimes of training for each method, excluding hyper-parameters validation. d is the dimension of the state-space. N is the total number of samples in all the trajectories. q is the number of features. T is the number of epochs. k_1 and k_2 are constant.

Schlather (2012), as well to the development of Gaussian processes constrained by PDEs Harkonen et al. (2023); Henderson et al. (2023) in recent years. We will demonstrate how the occupation kernel method can be adapted to ensure that the recovered vector field analytically satisfies the divergence-free/curl-free constraint for an appropriate choice of matrix kernel K . Then, for ease of presentation, we will apply just the divergence-free kernels to both real and synthetic datasets.

5.1 Divergence-free kernels

Let $x \in \mathbb{R}^d$ and $d = 2, 3$, and let $\phi(\|x\|)$ be a radial basis function. Then the standard construction Fuselier (2008) for divergence-free and curl-free matrix-valued radial basis functions are

$$\{-\Delta I + \nabla \nabla^T\} \phi(\|x\|) \quad \text{and} \quad -\nabla \nabla^T \phi(\|x\|), \quad (29)$$

respectively, where $\Delta = \sum_{i=1}^d \partial^2 / \partial x_i^2$ and $[\nabla \nabla^T]_{ij} = \partial^2 / \partial x_i \partial x_j$, $1 \leq i, j \leq d$. For example, if $d = 2$, then

$$\{-\Delta I + \nabla \nabla^T\} \phi(\|x\|) = \begin{bmatrix} -\frac{\partial^2 \phi}{\partial x_1^2} & \frac{\partial^2 \phi}{\partial x_1 \partial x_2} \\ \frac{\partial^2 \phi}{\partial x_2 \partial x_1} & -\frac{\partial^2 \phi}{\partial x_2^2} \end{bmatrix} (\|x\|). \quad (30)$$

Thus, the columns of the matrix-valued radial basis function $\{-\Delta I + \nabla \nabla^T\} \phi(\|x\|)$ are divergence-free. Similarly, we have that the columns of $-\nabla \nabla^T \phi(\|x\|)$ are curl-free.

We select the divergence-free kernel $K(x, y) = \{-\Delta I + \nabla \nabla^T\} \phi(\|x - y\|)$ where our choice of scalar radial basis function is the C^{10} Matérn kernel Fuselier et al. (2016).

5.2 Hamiltonian systems

A system

$$\dot{x}_1 = f(x_1, x_2), \quad \dot{x}_2 = g(x_1, x_2) \quad (31)$$

is called a *Hamiltonian system* if there exists a function $H(x_1, x_2)$ (called the *Hamiltonian*) for which $f = \partial H / \partial x_2$ and $g = -\partial H / \partial x_1$. This implies that the vector field (f, g) is divergence-free. Furthermore, along every orbit we have $H(x_1, x_2) = \text{constant}$ and any conservative dynamical equation $\ddot{u} = f(u)$ leads to a Hamiltonian system where the Hamiltonian coincides with the total energy. For example, every orbit of the conservative system corresponding to the equation describing the motion of a pendulum

$$\dot{x}_1 = x_2, \quad \dot{x}_2 = -\frac{g}{\ell} \sin(x_1) \quad (32)$$

satisfies the conservation law

$$H(x_1, x_2) = \frac{1}{2}x_2^2 - \frac{g}{\ell} \cos(x_1) = E \quad (33)$$

for some constant E .

5.3 Experiments

We test the divergence-free MOCK method on the following real and synthetic datasets.

Pendulum Problem We generate data using (32) with $\ell = 1$ and $g = 9.8$. This 2-dimensional synthetic dataset consists of 100 trajectories of 50 samples each. This dataset allows us to test whether the MOCK method can, simultaneously, learn a known Hamiltonian system while analytically enforcing the divergence free constraint.

Buoy Data We obtained a buoy dataset from <https://oceanofthings.darpa.mil/data#tab-all>, which contains two-dimensional trajectories of buoys submerged in the ocean. We sampled every tenth observation of the raw data and converted the time measurements into years. Trajectories with only one sample were dropped.

5.4 Evaluation

The error was computed using (28) for both datasets. For the pendulum problem, the scalar Matérn kernel provided an error of 1.5×10^{-1} while the divergence-free kernel provided an error of 1.9×10^{-2} , an improvement by an order of magnitude. Not only does the divergence-free kernel allow for a physically constrained solution, but it is also more accurate. For the buoy data, the scalar Matérn kernel provided an error of 3.5×10^1 while the divergence-free kernel provided an error of 3.1×10^1 . Thus, despite the presence of noise (which is not necessarily divergence-free), we still achieve a reduction in the error of about 10%.

Figure 5 shows the error in the computed vector fields of the pendulum problem. A plot of the results for the buoy data problem using the divergence-free kernel, along with the training data, is shown in figure 6.

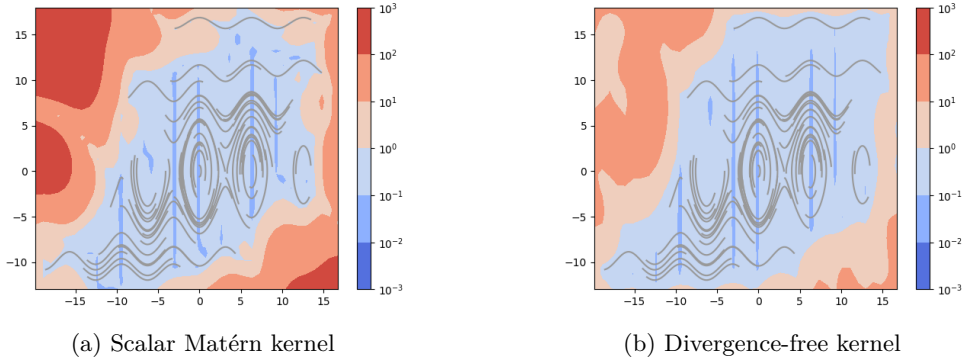


Figure 5: The magnitude of the error in vector field approximation of the pendulum problem obtained using different choices of kernel along with the training set (gray).

6 Summary and discussion

The implicit matrix-valued kernel formulation has enabled us to demonstrate that the MOCK algorithm, originally proposed by J. Rosenfeld and collaborators, effectively learns the vector field of an ODE in multivariate settings or under predefined constraints, while maintaining linear scalability with the dimension of the state space. We have benchmarked the algorithm against a representative selection of competitive methods and provided compelling experimental evidence showcasing its superior performance on many datasets, along with consistently competitive results across all cases tested.

A rigorous analysis of the algorithm's convergence and error, including precise assumptions regarding noise, is deferred to future work. This analysis will incorporate the quadrature error and the effects of noise, as well as provide concentration inequalities to quantify the error between predicted and true trajectories as functions of quadrature precision, observation noise levels, and data granularity, offering insights into the algorithm's generalization capabilities.

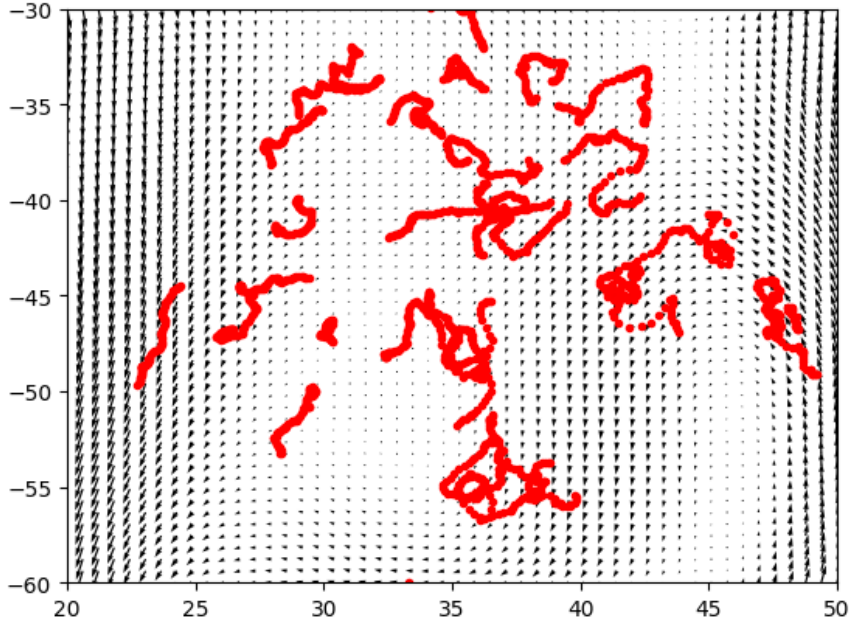


Figure 6: A detail of the vector field learned using the divergence-free kernel from the buoy data together with the training set (red).

The surprising simplicity of the MOCK technique, combined with its strong performance, opens the door to numerous opportunities for optimization, generalization, and further exploration. Future work is expected to advance the state-of-the-art in high-dimensional dynamics learning, extend applications to PDEs, and analyze generalization properties in detail.

References

Joseph Bakarji, Kathleen Champion, J Nathan Kutz, and Steven L Brunton. Discovering governing equations from partial measurements with deep delay autoencoders. *arXiv preprint arXiv:2201.05136*, 2022.

Steven L Brunton, Joshua L Proctor, and J Nathan Kutz. Discovering governing equations from data by sparse identification of nonlinear dynamical systems. *Proceedings of the national academy of sciences*, 113(15):3932–3937, 2016.

Kathleen Champion, Bethany Lusch, J Nathan Kutz, and Steven L Brunton. Data-driven discovery of coordinates and governing equations. *Proceedings of the National Academy of Sciences*, 116(45):22445–22451, 2019.

Ricky TQ Chen, Yulia Rubanova, Jesse Bettencourt, and David K Duvenaud. Neural ordinary differential equations. *Advances in neural information processing systems*, 31, 2018.

Anthony M DeGennaro and Nathan M Urban. Scalable extended dynamic mode decomposition using random kernel approximation. *SIAM Journal on Scientific Computing*, 41(3):A1482–A1499, 2019.

Kathryn P. Drake, Edward J. Fuselier, and Grady B. Wright. Implicit surface reconstruction with a curl-free radial basis function partition of unity method. *SIAM Journal on Scientific Computing*, 44(5):A3018–A3040, 2022. doi: 10.1137/22M1474485.

Urban Fasel, J Nathan Kutz, Bingni W Brunton, and Steven L Brunton. Ensemble-sindy: Robust sparse model discovery in the low-data, high-noise limit, with active learning and control. *Proceedings of the Royal Society A*, 478(2260):20210904, 2022.

Gregory E. Fasshauer and Michael J. McCourt. *Kernel-based Approximation Methods using MATLAB*. World Scientific, New Jersey, 2015.

Richard FitzHugh. Impulses and physiological states in theoretical models of nerve membrane. *Biophysical journal*, 1(6):445–466, 1961.

E. Fuselier, V. Shankar, and G. Wright. A high-order radial basis function (rbf) leray projection method for the solution of the incompressible unsteady stokes equations. *Computers and Fluids*, 128:41–52, 2016.

E. J. Fuselier. Sobolev-type approximation rates for divergence-free and curl-free rbf interpolants. *Math. Comput.*, 77:1407–1423, 2008.

E. J. Fuselier and G. B. Wright. Stability and error estimates for vector field interpolation and decomposition on the sphere with rbfs. *SIAM J. Num. Anal.*, 47:3213–3239, 2009.

W. W. Gao, G. E. Fasshauer, and N. Fisher. Divergence-free quasi-interpolation. *Appl. Comp. Harmon. Anal.*, 60:471–488, 2022.

Amnon Geifman, Abhay Yadav, Yoni Kasten, Meirav Galun, David Jacobs, and Basri Ronen. On the similarity between the laplace and neural tangent kernels. *Advances in Neural Information Processing Systems*, 33:1451–1461, 2020.

Marc Harkonen, Markus Lange-Hegermann, and Bogdan Raita. Gaussian Process Priors for Systems of Linear Partial Differential Equations with Constant Coefficients. In *Proceedings of the 40th International Conference on Machine Learning*, pp. 12587–12615. PMLR, July 2023.

Kaiming He, Xiangyu Zhang, Shaoqing Ren, and Jian Sun. Deep residual learning for image recognition. In *Proceedings of the IEEE conference on computer vision and pattern recognition*, pp. 770–778, 2016.

Iain Henderson, Pascal Noble, and Olivier Roustant. Characterization of the second order random fields subject to linear distributional PDE constraints. *Bernoulli*, 29(4):3396–3422, November 2023. doi: 10.3150/23-BEJ1588.

Sterling C Johnson, Rebecca L Koscik, Erin M Jonaitis, Lindsay R Clark, Kimberly D Mueller, Sara E Berman, Barbara B Bendlin, Corinne D Engelman, Ozioma C Okonkwo, Kirk J Hogan, et al. The wisconsin registry for alzheimer’s prevention: a review of findings and current directions. *Alzheimer’s & Dementia: Diagnosis, Assessment & Disease Monitoring*, 10:130–142, 2018.

Kadierdan Kaheman, J Nathan Kutz, and Steven L Brunton. Sindy-pi: a robust algorithm for parallel implicit sparse identification of nonlinear dynamics. *Proceedings of the Royal Society A*, 476(2242):20200279, 2020.

Kamel Lahouel, Michael Wells, David Lovitz, Victor Rielly, Ethan Lew, and Bruno Jedynak. Learning nonparametric ordinary differential equations: Application to sparse and noisy data. *arXiv preprint arXiv:2206.15215*, 2022.

Ethan Lew, Abdelrahman Hekal, Kostiantyn Potomkin, Niklas Kochdumper, Brandon Hencsey, Stanley Bak, and Sergiy Bogomolov. Autokoopman: A toolbox for automated system identification via koopman operator linearization. In *International Symposium on Automated Technology for Verification and Analysis (ATVA)*, 2023. Under review.

Yunzhu Li, Hao He, Jiajun Wu, Dina Katabi, and Antonio Torralba. Learning compositional koopman operators for model-based control. *arXiv preprint arXiv:1910.08264*, 2019.

Edward N Lorenz. Deterministic nonperiodic flow. *Journal of atmospheric sciences*, 20(2):130–141, 1963.

E.N. Lorenz. Predictability: a problem partly solved. In *Seminar on Predictability*, volume 1, pp. 1–18, Shinfield Park, Reading, 1995. ECMWF.

S. Lowitzsch. Error estimates for matrix-valued radial basis function interpolation. *Journal of Approximation Theory*, 137:238–249, 2005.

Lu Lu, Xuhui Meng, Zhiping Mao, and George Em Karniadakis. Deepxde: A deep learning library for solving differential equations. *SIAM review*, 63(1):208–228, 2021.

Bethany Lusch, J Nathan Kutz, and Steven L Brunton. Deep learning for universal linear embeddings of nonlinear dynamics. *Nature communications*, 9(1):4950, 2018.

Colin P McNally. Divergence-free interpolation of vector fields from point values—exact $\nabla \cdot \mathbf{B} = 0$ in numerical simulations. *Monthly Notices of the Royal Astronomical Society: Letters*, 413(1):L76–L80, 2011.

Frederick Mosteller and R. A. Fisher. Questions and answers. *The American Statistician*, 2(5):30–31, 1948. ISSN 00031305. URL <http://www.jstor.org/stable/2681650>.

F. Narcowich and J. Ward. Generalized hermite interpolation via matrix-valued conditionally positive definite functions. *Mathematics of Computation*, 63:661–688, 1994.

F. Narcowich, J. Ward, and G. B. Wright. Divergence-free rbfs on surfaces. *J. Fourier Anal. Appl.*, 13: 643–663, 2007.

Konrad Polthier and Eike Preuß. Identifying vector field singularities using a discrete hodge decomposition. In Hans-Christian Hege and Konrad Polthier (eds.), *Visualization and Mathematics III*, pp. 113–134, Berlin, Heidelberg, 2003. Springer Berlin Heidelberg.

Ali Rahimi and Benjamin Recht. Random features for large-scale kernel machines. In *Neural Information Processing Systems*, 2007. URL <https://api.semanticscholar.org/CorpusID:877929>.

Joel A Rosenfeld, Rushikesh Kamalapurkar, Benjamin Russo, and Taylor T Johnson. Occupation kernels and densely defined liouville operators for system identification. In *2019 IEEE 58th Conference on Decision and Control (CDC)*, pp. 6455–6460. IEEE, 2019a.

Joel A Rosenfeld, Benjamin Russo, Rushikesh Kamalapurkar, and Taylor T Johnson. The occupation kernel method for nonlinear system identification. *arXiv preprint arXiv:1909.11792*, 2019b.

Joel A. Rosenfeld, Benjamin P. Russo, Rushikesh Kamalapurkar, and Taylor T. Johnson. The occupation kernel method for nonlinear system identification. *SIAM Journal on Control and Optimization*, 62(3): 1643–1668, 2024. doi: 10.1137/19M127029X. URL <https://doi.org/10.1137/19M127029X>.

Yulia Rubanova, Ricky TQ Chen, and David K Duvenaud. Latent ordinary differential equations for irregularly-sampled time series. *Advances in neural information processing systems*, 32, 2019.

Benjamin P Russo, Rushikesh Kamalapurkar, Dongsik Chang, and Joel A Rosenfeld. Motion tomography via occupation kernels. *arXiv preprint arXiv:2101.02677*, 2021.

Michael Scheuerer and Martin Schlather. Covariance models for divergence-free and curl-free random vector fields. *Stochastic Models*, 28(3):433–451, 2012. doi: 10.1080/15326349.2012.699756. URL <https://doi.org/10.1080/15326349.2012.699756>.

Bernhard Schölkopf and Alexander J. Smola. *Learning with kernels : support vector machines, regularization, optimization, and beyond*. Adaptive computation and machine learning. MIT Press, 2002. URL <http://www.worldcat.org/oclc/48970254>.

Jonathan H Tu. *Dynamic mode decomposition: Theory and applications*. PhD thesis, Princeton University, 2013.

Niklas Wahlström, Manon Kok, Thomas B. Schön, and Fredrik Gustafsson. Modeling magnetic fields using gaussian processes. In *2013 IEEE International Conference on Acoustics, Speech and Signal Processing*, pp. 3522–3526, 2013. doi: 10.1109/ICASSP.2013.6638313.

H. Wendland. Divergence-free kernel methods for approximating the stokes problem. *SIAM J. Numer. Anal.*, 47:3158–3179, 2009.

Matthew O Williams, Ioannis G Kevrekidis, and Clarence W Rowley. A data–driven approximation of the koopman operator: Extending dynamic mode decomposition. *Journal of Nonlinear Science*, 25:1307–1346, 2015.

Enoch Yeung, Soumya Kundu, and Nathan Hudas. Learning deep neural network representations for koopman operators of nonlinear dynamical systems. In *2019 American Control Conference (ACC)*, pp. 4832–4839. IEEE, 2019.

A Experiment Code

We created a code capsule on Code Ocean that hosts all the methods used in our experiments for system identification of ordinary differential equations. The code repository allows for the repeatability of our results for a single experiment—Lorenz63—and facilitates the evaluation of the performance of different models on synthetic and real-world datasets. The real world plasma and imaging experiment are restricted data and will not be available for the evaluation.

We provide an *anonymized* zipfile (6.6 MB) export of the code capsule for review at <https://drive.google.com/file/d/1p36HH00dHGLuBeHEfhJyM1fxjv1At5La/view?usp=sharing>. The code can be run locally in a Docker container with instructions in the README.md and REPRODUCING.md.

To ensure the reproducibility of the experiment, we have tuned the hyperparameters for each method, except for ResNet, which is known to require substantial tuning time. The code repository provides detailed instructions for running each method experiment, including the necessary input data and the corresponding hyperparameter settings. Please note that due to limitations on Code Ocean, we have set the TensorFlow library to use the CPU rather than the GPU, as using the GPU resulted in numerous errors. This may increase the runtime of the experiments. For the paper, we ran some experiments in google colab on A100 GPUs where the training time was much lower.

Upon running the code repository, the experiments will take approximately 1.5 hours to complete. The results of each experiment are provided in the form of trajectory CSV files, capturing the predicted trajectories of the identified systems. These trajectory files can be further analyzed or visualized as desired. Additionally, a summary of the performance of each method is available in the code repository.

B Datasets

B.1 Synthetic data

Noisy FitzHugh-Nagumo The FitzHugh-Nagumo oscillator FitzHugh (1961) is a nonlinear 2D dynamical system that models the basic behavior of excitable cells, such as neurons and cardiac cells (See figure 3). The system is popular in the analysis of dynamical systems for its rich behavior, including relaxation oscillations and bifurcations. The FHN oscillator consists of two coupled ODEs that describe the membrane potential v and recovery variable w ,

$$\dot{v} = v - \frac{v^3}{3} - w + RI \quad (34)$$

$$\tau \dot{w} = v + a - bw \quad (35)$$

Here, I is the external current input, a and b are positive constants that affect the shape and duration of the action potential, and τ is the time constant that determines the speed of the recovery variable’s response. We added random Gaussian noise of standard deviation 0.12 to this dataset.

Noisy Lorenz63 The 3D Lorenz 63 system Lorenz (1963) is a simplified model of atmospheric convection, but has since become a canonical example of chaos in dynamical systems. The Lorenz 63 system exhibits sensitive dependence on initial conditions and parameters, which gives rise to its characteristic butterfly-shaped

chaotic attractor. The equations are

$$\begin{aligned}\frac{dx}{dt} &= \sigma(y - x) \\ \frac{dy}{dt} &= x(\rho - z) - y. \\ \frac{dz}{dt} &= xy - \beta z\end{aligned}\tag{36}$$

Here, x , y , and z are state variables representing the fluid's convective intensity, and σ , ρ , and β are positive parameters representing the Prandtl number, the Rayleigh number, and a geometric factor, respectively. We added random Gaussian noise with standard deviation 0.5 to this dataset.

Lorenz96 The Lorenz96 data arises from Lorenz (1995) in which a system of equations is proposed that may be chosen to have any dimension greater than 3. The chaotic system is defined by:

$$\frac{dx_k}{dt} = -x_{k-1}x_{k-2} + x_{k+1}x_{k-1} - x_k + F\tag{37}$$

where we take $F = 8$ and consider 16, 32, 128 and 1024 dimensional systems. Indices are assumed to wrap so that for an n dimensional system $x_{-2} = x_{n-2}$.

B.2 Real Data

CMU Walking The Carnegie Mellon University (CMU) Walking data is a repository of publicly available data. It can be found at <http://mocap.cs.cmu.edu/>. It was generated by placing sensors on a number of subjects and recording the position of the sensors as the subjects walked forward by a fixed amount and then walked back. There were 50 spatial dimensions of data as recorded by the sensors, which were recorded at regular times. Since the observation times were not provided, we separated each observation in time by 0.1 units and began each trajectory at time zero. The CMU Walking data which we used for our experiments consists of 75 trajectories with an average of 106.7 observations per trajectory. We could not use the full amount of data provided because some subjects did not walk in the same manner as other subjects.

It should be noted that it may not be appropriate to consider the CMU walking data as being generated by a single dynamical system. Since there were multiple subjects in the dataset, it is reasonable to conclude that there are multiple dynamical systems responsible for the motion of these different subjects. However, we fit our model to this dataset assuming that it was generated by a single dynamical system.

Plasma This dataset includes imaging and plasma biomarkers from the WRAP study, see Johnson et al. (2018). The imaging biomarker is a distribution volume ratio obtained from Pittsburgh Compound-B positron emission tomography. The plasma biomarkers include $A\beta_{40}/A\beta_{42}$ that reflects specific amyloid beta ($A\beta$) proteoforms; ptau217, which has a high correlation with amyloid PET positivity, GFAP, which measures the levels of the astrocytic intermediate filament glial fibrillary acidic protein, and NFL, a recognized biomarker of subcortical large-caliber axonal degeneration, for a total of 6 biomarkers. There are a total $n = 425$ trajectories, one per subject, and, on average, 2.95 time points per trajectory. The data was split (70%, 10%, 20%) corresponding resp. to training, validation, and testing.

Imaging This dataset includes regional imaging biomarkers from the WRAP study, see Johnson et al. (2018). The imaging biomarker is an atlas-based distribution volume ratio obtained from Pittsburgh Compound-B positron emission tomography. There are a total of 117 biomarkers. There are a total of $n = 231$ trajectories, one per subject, and, on average, 2.26 time points per trajectory. The data was split (70%, 10%, 20%) corresponding resp. to training, validation, and testing.

C Reproducing Kernel Hilbert Spaces (RKHS)

Basic notions and notations associated with RKHSs are important for understanding the algorithms presented in this paper. We thus provide a short presentation. We limit ourselves to RKHSs over the field of real

numbers. RKHSs are Hilbert spaces for which the evaluation functional is continuous. The evaluation functional at $x \in \mathbb{R}$ is a mapping from an RKHS \mathbb{H} to \mathbb{R} , which associates to a function its evaluation at x , that is $f \mapsto f(x)$. Riesz representation theorem allows us to interpret evaluations of a function in an RKHS as a geometric operation consisting of computing an inner product. That is, there is a unique vector $k_x \in \mathbb{H}$ such that $f(x) = \langle f, k_x \rangle$. Moreover, let us define, for any $x, y \in \mathbb{R}$, the so-called kernel $k(x, y) = \langle k_x, k_y \rangle$. Let us use this to characterize the function k_x . Evaluating k_x at y and using Riesz representation provides $k_x(y) = \langle k_x, k_y \rangle = \langle k_y, k_x \rangle = k(y, x)$. Thus the function $k_x(\cdot)$ is the function $k(\cdot, x)$. Moreover, for any $f \in \mathbb{H}$, $f(x) = \langle f, k(\cdot, x) \rangle$. This is the reproducing property of the kernel. Applying this property to k_y implies that $k(x, y) = \langle k(\cdot, x), k(\cdot, y) \rangle$

C.1 Linear functionals and occupation kernels

Let \mathbb{H} be an RKHS of functions from \mathbb{R} to \mathbb{R} with kernel k . Assume that $x \mapsto k(x, x)$ is continuous. Consider a continuous parametric curve $[0, 1] \rightarrow \mathbb{R}$, $t \mapsto x(t)$ and define the functional from an RKHS \mathbb{H} to \mathbb{R} , $L_x(f) = \int_0^1 f(x(t))dt$. L_x is clearly linear. The Cauchy-Schwarz inequality implies L_x is bounded. Indeed,

$$|L_x(f)| = \left| \int_0^T f(x(t))dt \right| \quad (38)$$

$$= \left| \int_0^T \langle f, k(\cdot, x(t)) \rangle dt \right| \quad (39)$$

$$\leq \int_0^T |\langle f, k(\cdot, x(t)) \rangle| dt \quad (40)$$

$$\leq \int_0^T \|f\| \|k(\cdot, x(t))\| dt \quad (41)$$

$$= \|f\| \int_0^T \sqrt{k(x(t), x(t))} dt \quad (42)$$

where we have used the Cauchy-Schwartz inequality in (41). Now, since $t \mapsto x(t)$ and $x \mapsto k(x, x)$ are continuous, the integral in (42) is upper-bounded. Thus the functional $L_x(f)$ is continuous.

We use Riesz representation theorem to define the occupation kernel function as the unique element L_x^* in \mathbb{H} that verifies $L_x(f) = \langle f, L_x^* \rangle$. Note that

$$L_x^*(y) = \langle L_x^*, k(\cdot, y) \rangle = \langle k(\cdot, y), L_x^* \rangle = L_x(k(\cdot, y)) = \int_0^1 k(x(t), y) dt \quad (43)$$

Furthermore,

$$\langle L_x^*, L_y^* \rangle = L_y(L_x^*) = \int_0^1 L_x^*(y(t)) dt = \int_0^1 \int_0^1 k(x(s), y(t)) ds dt \quad (44)$$

C.2 Kernels

For all experiments (except for section 5) we use standard scalar-valued positive definite kernels, references to which may be found, see, for example, Table 3.1 on page 42 of Fasshauer & McCourt (2015). Additionally, in section 5, we demonstrate how a divergence-free kernel allows us to incorporate physical constraints in our model. The specific divergence-free kernel we use is given in Fuselier et al. (2016). For the sake of clarity, we include the analytical forms of the kernels used throughout the paper below:

Guassian kernel:

$$g(x, y, \sigma) = \exp \left(-\frac{\|x - y\|^2}{2\sigma^2} \right) \quad (45)$$

Laplace kernel:

$$l(x, y, \gamma) = \exp\left(-\frac{\|x - y\|}{\gamma}\right) \quad (46)$$

Fourier Feature kernel:

$$f(x, y, \sigma) = \frac{1}{\sqrt{q}} [cos(z_1^T x / \sigma + \beta_1), \dots, cos(z_q^T x / \sigma + \beta_q)]^T [cos(z_1^T y / \sigma + \beta_1), \dots, cos(z_q^T y / \sigma + \beta_q)] \quad (47)$$

Matérn kernel C^{10} :

$$m(x, y, \sigma) = \frac{1}{945} \exp(-r/\sigma) \left(\left(\frac{r}{\sigma}\right)^5 + 15 \left(\frac{r}{\sigma}\right)^4 + 105 \left(\frac{r}{\sigma}\right)^3 + 420 \left(\frac{r}{\sigma}\right)^2 + 945 \left(\frac{r}{\sigma}\right) + 945 \right) \quad (48)$$

where in equation 47 $z_i \sim N(0, I)$ and $\beta_i \sim U(0, 2\pi)$, and in equation 48 $r = \|x - y\|$. We now introduce the divergence-free kernel of section 5. Let

$$d_1(x, y, \sigma) = \frac{-1}{945\sigma^2} \exp(-r/\sigma) \left(\left(\frac{r}{\sigma}\right)^4 + 10 \left(\frac{r}{\sigma}\right)^3 + 45 \left(\frac{r}{\sigma}\right)^2 + 105 \left(\frac{r}{\sigma}\right) + 105 \right)$$

and

$$d_2(x, y, \sigma) = \frac{1}{945\sigma^4} \exp(-r/\sigma) \left(\left(\frac{r}{\sigma}\right)^3 + 6 \left(\frac{r}{\sigma}\right)^2 + 15 \left(\frac{r}{\sigma}\right)^2 + 15 \right),$$

and define

$$\phi_{11}(x, y, \sigma) = -d_2(x, y, \sigma)(x_2 - y_2)^2 - d_1(x, y, \sigma),$$

$$\phi_{22}(x, y, \sigma) = -d_2(x, y, \sigma)(x_1 - y_1)^2 - d_1(x, y, \sigma),$$

and

$$\phi_{12}(x, y, \sigma) = \phi_{21}(x, y, \sigma) = d_2(x, y, \sigma)(x_1 - y_1)(x_2 - y_2),$$

where $x = [x_1, x_2]^T$, $y = [y_1, y_2]^T$, and $r = \|x - y\|$. Then,

$$m_{div}(x, y, \sigma) = \begin{bmatrix} \phi_{11} & \phi_{12} \\ \phi_{21} & \phi_{22} \end{bmatrix} (x, y, \sigma). \quad (49)$$

D Vector-Valued Reproducing Kernel Hilbert Spaces

There are three ways to characterize a vvRKHS.

Firstly, we can construct a vvRKHS with linear functions of the kernel:

Definition 3. Let

$$\mathbb{H}_0 = \left\{ f; f(x) = \sum_{i=1}^n K(x, x_i) w_i, x_i \in \mathcal{X}, w_i \in \mathbb{R}^d, i = 1 : n \right\} \quad (50)$$

then, consider the encoding in \mathbb{H}_0 of the functions f and g ,

$$f \longleftrightarrow \begin{cases} x_1, \dots, x_n \\ w_1, \dots, w_n \end{cases} \quad \text{and} \quad g \longleftrightarrow \begin{cases} y_1, \dots, y_m \\ v_1, \dots, v_m \end{cases} \quad (51)$$

Define the inner product

$$\langle f, g \rangle = \sum_{i=1}^n \sum_{j=1}^m w_i^T K(x_i, y_j) v_j \quad (52)$$

then the closure of \mathbb{H}_0 for $\langle \cdot, \cdot \rangle$ is the vvRKHS of K .

The second construction starts from a Hilbert space and uses the Riesz representation theorem.

Definition 4. Let \mathbb{H} be a Hilbert space of functions $\mathbb{R}^d \rightarrow \mathbb{R}^d$ such that for any $x \in \mathbb{R}^d$, the evaluation functional $f \mapsto f(x)$ is continuous: there is a constant $M_x \in \mathbb{R}$, such that

$$\|f(x)\|_{\mathbb{R}^d} \leq M_x \|f\|_{\mathbb{H}} \quad (53)$$

for all $f \in \mathbb{H}$. Then, using the Riesz representation, for any $v \in \mathbb{R}^d$ there exists a unique $K_{x,v} \in \mathbb{H}$ such that

$$v^T f(x) = \langle f, K_{x,v} \rangle_{\mathbb{H}} \quad (54)$$

This equation is the *reproducing property*.

Define the matrix-valued kernel

$$K_{ij}(x, x') = \langle K_{x,e_i}, K_{x',e_j} \rangle, i, j = 1 \dots d \quad (55)$$

where e_1, \dots, e_d is the natural basis of \mathbb{R}^d . Then K is a kernel and \mathbb{H} is the vvRKHS of K .

The third formulation allows for checking that a Hilbert space is a vvRKHS.

Definition 5. Let \mathbb{H} be a Hilbert space of functions $\mathbb{R}^d \rightarrow \mathbb{R}^d$. Let K be a (d, d) matrix-valued kernel. \mathbb{H} is the vvRKHS of K when

1. For any $x' \in \mathcal{X}$, $v \in \mathbb{R}^d$, $x \mapsto K(x, x')v \in \mathbb{H}$
2. The reproducing property holds: for any $f \in \mathbb{H}$, $x \in \mathcal{X}$, $v \in \mathbb{R}^d$, equation 54 holds

D.1 Verifying the continuity for the occupation kernel in multiple dimensions

Let $(e_1, \dots, e_d)^T$ be the standard basis of \mathbb{R}^d . Then

$$|e_j^T L_x(f)| = \left| \int_0^T e_j^T f(x(t)) dt \right| \quad (56)$$

$$\leq \int_0^T |e_j^T f(x(t))| dt \quad (57)$$

$$= \int_0^T |\langle f, K(., x(t)) e_j \rangle| dt \quad (58)$$

$$\leq \|f\| \int_0^T \sqrt{K_{jj}(x(t), x(t))} dt \quad (59)$$

where we have used the Cauchy-Schwartz inequality. If $x \mapsto K_{jj}(x, x)$ is continuous, then since $t \mapsto x(t)$ is continuous, $e_j^T L_x$ is bounded for each $1 \leq j \leq d$, which implies that L_x is bounded and thus continuous.

D.2 Occupation Kernel inner product

Consider

$$L_{x,v}^*(\cdot) = \int_0^T K(\cdot, x(t)) dt v$$

$$L_{y,w}^*(\cdot) = \int_0^T K(\cdot, y(t)) dt w$$

we wish to evaluate

$$\langle L_{x,v}^*, L_{y,w}^* \rangle = w^T L_y (L_{x,v}^*(\cdot)) \quad (60)$$

$$= w^T \int_0^T \left\{ \int_0^T K(y(s), x(t)) dt v \right\} ds \quad (61)$$

$$= w^T \left(\int_0^T \int_0^T K(y(s), x(t)) dt ds \right) v \quad (62)$$

E Proof of Theorem 1

Consider the linear span of the occupation kernel functions $L_{x_i, \alpha_i}^*, i = 1 \dots n$

$$\mathcal{F} = \left\{ f \in \mathbb{H}, f = \sum_{i=1}^n L_{x_i, \alpha_i}^*, \alpha = (\alpha_1, \dots, \alpha_n) \in \mathbb{R}^{d \times n} \right\} \quad (63)$$

Note that \mathcal{F} is linear and finite-dimensional; thus, it is a closed linear subspace of \mathbb{H} . We can then project any function in \mathbb{H} orthogonally onto it

$$f = f_{\mathcal{F}} + f_{\mathcal{F}^\perp} \quad (64)$$

Now, for each $i = 1 \dots n$, and $v \in \mathbb{R}^d$,

$$v^T \int_{a_i}^{b_i} f(x_i(t)) dt = v^T L_{x_i}(f) = \langle L_{x_i, v}^*, f \rangle = \langle L_{x_i, v}^*, f_{\mathcal{F}} + f_{\mathcal{F}^\perp} \rangle = \langle L_{x_i, v}^*, f_{\mathcal{F}} \rangle \quad (65)$$

where the previous to last equality comes from the fact that $f_{\mathcal{F}^\perp}$ is perpendicular to $L_{x_i, v}^*$. Thus,

$$\int_{a_i}^{b_i} f(x_i(t)) dt = L_{x_i}(f_{\mathcal{F}}) \quad (66)$$

Next, using the Pythagorean equality

$$\|f\|^2 = \|f_{\mathcal{F}}\|^2 + \|f_{\mathcal{F}^\perp}\|^2 \geq \|f_{\mathcal{F}}\|^2 \quad (67)$$

Thus, for any $f \in \mathbb{H}$, $J(f_{\mathcal{F}}) \leq J(f)$ which proves that the minimum of J actually belongs to \mathcal{F} . Moreover, note that

$$\begin{aligned} \|f_{\mathcal{F}}\|^2 &= \left\langle \sum_{i=1}^n L_{x_i, \alpha_i}^*, \sum_{i=1}^n L_{x_i, \alpha_i}^* \right\rangle = \sum_{i,j=1}^n \langle L_{x_i, \alpha_i}^*, L_{x_j, \alpha_j}^* \rangle \\ &= \sum_{i,j=1}^n \alpha_i^T \left[\int_{a_i}^{b_i} \int_{a_j}^{b_j} K(x_i(s), x_j(t)) ds dt \right] \alpha_j = \sum_{i,j=1}^n \alpha_i^T M_{ij} \alpha_j = \alpha^T M \alpha \end{aligned} \quad (68)$$

Also,

$$L_{x_i}(f_{\mathcal{F}}) = L_{x_i} \left(\sum_{j=1}^n L_{x_j, \alpha_j}^* \right) \quad (69)$$

$$= \int_{a_i}^{b_i} \sum_{j=1}^n L_{x_j, \alpha_j}^*(x_i(t)) dt \quad (70)$$

$$= \sum_{j=1}^n \left[\int_{a_i}^{b_i} \int_{a_j}^{b_j} K(x_i(t), x_j(s)) ds dt \right] \alpha_j \quad (71)$$

$$= \sum_{j=1}^n M_{ij} \alpha_j \quad (72)$$

$$= [M\alpha]_i \quad (73)$$

The minimization problem in f is thus equivalent to minimizing in α

$$J(\alpha) = \frac{1}{n} \sum_{i=1}^n \| [M\alpha]_i - x_i(b_i) + x_i(a_i) \|_{\mathbb{R}^d}^2 + \lambda \alpha^T M \alpha \quad (74)$$

or equivalently,

$$J(\alpha) = \frac{1}{n} \| M\alpha - x(b) + x(a) \|_{\mathbb{R}^{nd}}^2 + \lambda \alpha^T M \alpha \quad (75)$$

since $\lambda > 0$ and M is PSD, this is solved by

$$(M + \lambda n I) \alpha = x(b) - x(a) \quad (76)$$

F Computational Complexity

We detail below an analysis of the complexity for MOCK in terms of d , the dimension of the state space, and N , the total number of observations. We present the implicit and explicit kernels successively.

F.1 Implicit kernel

In several of our experiments, an implicit Gaussian kernel was used. The Gram matrix for the kernel is $N \times m$ where N is the total number of samples in the dataset X and m is the total number of samples in the dataset Y . If $X \in \mathbb{R}^{d \times N}$, and $Y \in \mathbb{R}^{d \times m}$, we may compute any radial basis function kernel defined by:

$$G_{i,j} = f(\|x_i - y_j\|^2) \quad (77)$$

by observing:

$$D = \text{outer}(\text{sum}(X \circledast X), 1_m) - 2X^T Y + \text{outer}(1_N, \text{sum}(Y \circledast Y)) \quad (78)$$

Where $D_{i,j} = \|X_i - Y_j\|^2$ is the matrix of square distances, \circledast is the Hadamard product, sum is column sum, outer is an outer product, and 1_N is the ones vector in N dimensions. $G \in \mathbb{R}^{N \times N}$ is then calculated by applying f component by component to D for the training set X with X . The computational bottleneck of this Gram matrix computation is the $N \times d$ by $d \times m$ matrix matrix multiplication, with a worst case run time that is $O(dNm) = O(dN^2)$ when $Y = X$ (with a naive implementation of matrix matrix multiplication).

We integrate over intervals of a single pair of samples, and these integrals are estimated using the trapezoid rule quadrature. Therefore, for instance, if a single trajectory is given, we would get our estimate of all our integrals by simply taking the matrix

$$k = \frac{h^2}{4} \begin{bmatrix} 1 & 1 \\ 1 & 1 \end{bmatrix} \quad (79)$$

and convolving it with the Gram matrix G . If multiple trajectories are given, we apply the same convolution to G and ignore terms involving sums that mix samples from different trajectories. In NumPy indexing notation, we may apply the above convolution with the expression:

$$M = \frac{h^2}{4} (G[1 :, 1 :] + G[: -1, 1 :] + G[1 :, : -1] + G[: -1, : -1]) \quad (80)$$

This adds an additional $O(N^2)$ computational complexity (for fixed $G \in \mathbb{R}^{N \times N}$).

Finally, the linear system we solve is:

$$(M + \lambda I) A = Y \quad (81)$$

Where $M \in \mathbb{R}^{N \times N}$ and $A, Y \in \mathbb{R}^{N \times d}$, which adds the dominating computational complexity term of $O(dN^3)$.

F.2 Explicit Kernel

Assuming the vvRKHS has a matrix-valued kernel of the form

$$K(x, y) = \psi(x)\psi^T(y) \quad (82)$$

where

$$\psi : \mathbb{R}^d \rightarrow \mathbb{R}^{d \times q} \quad (83)$$

we may recall:

$$f(x) = \sum_i \int_{a_i}^{b_i} \psi(x)\psi(x_i(\tau))^T d\tau \alpha_i = \psi(x) \sum_i \int_{a_i}^{b_i} \psi(x_i(\tau))^T d\tau \alpha_i = \psi(x)\beta \quad (84)$$

where $\beta \in \mathbb{R}^q$ is defined by $\beta = \sum_i \int_{a_i}^{b_i} \psi(x_i(\tau))^T d\tau \alpha_i$. Letting

$$\Psi \in \mathbb{R}^{Nd \times q} \quad (85)$$

be defined by:

$$\Psi_i \in \mathbb{R}^{d \times q} = \int_{a_i}^{b_i} \psi(x_i(\tau)) d\tau \quad (86)$$

Let

$$L^* = \Psi \Psi^T \quad (87)$$

then

$$\alpha^T L^* \alpha = \beta^T \beta. \quad (88)$$

Thus, we reduce the minimization problem 21 to

$$\min_{\beta} J(\beta) = \frac{1}{N} \sum_{i=1}^N \|[\Psi\beta]_i - x_i(b_i) + x_i(a_i)\|_{\mathbb{R}^d}^2 + \lambda \beta^T \beta \quad (89)$$

This simplifies to

$$(\Psi^T \Psi + \lambda N I) \beta = \Psi^T y \quad (90)$$

where $y \in \mathbb{R}^{Nd}$ with $y_i \in \mathbb{R}^d$ and $y_i = x_i(b_i) - x_i(a_i)$. Thus, in the explicit kernel case, we require evaluating Ψ which is $O(Ndq)$, a $q \times Nd$ by $Nd \times q$ matrix-matrix multiplication $O(q^2(Nd))$ and a $q \times q$ linear system solve which is $O(q^3)$. Notice, in the explicit kernel case, no assumptions on the overall structure of the kernel matrix $K(x, y)$ are needed. For instance, the matrices no longer need to be diagonal or proportional to the identity matrix. However, in practice, for best results, q will typically be dependent on the dimension d . If the kernel is I-separable however, the runtime may be improved. Indeed, supposing $\psi(x) = \phi(x) \otimes I \in \mathbb{R}^{pd}$ where $\phi : \mathbb{R}^d \rightarrow \mathbb{R}^p$. The runtime reduces from $O(q^2Nd + q^3) = O((pd)^2Nd + (pd)^3)$ to $O(p^2nd + p^3d)$

G Comparators:

The methods we benchmark against are presented in the table 4. References and hyperparameters are specified. The Null model is used as a baseline to determine that something was learned of the dataset. Our null model has no parameters and is the trivial dynamical system for which the slope-field is zero everywhere. A model that fails to outperform the null model likely did not learn any useful information about the dynamical system. We present now the computational complexity for each method.

Method	Hyperparameters
Null	N/A
Sparse Identification of Nonlinear Dynamics	
SINDy Brunton et al. (2016)	polynomial degree, sparsity threshold
Reduced Order Models	
eDMD-RFF DeGennaro & Urban (2019)	number of features, lengthscale
eDMD-Poly Williams et al. (2015)	polynomial degree
Deep Learning	
ResNet He et al. (2016) Lu et al. (2021)	network depth/breadth
eDMD-Deep Yeung et al. (2019)	latent space dimension, autoencoder depth/breadth
Latent Ode Rubanova et al. (2019)	latent space dimension, autoencoder and decoder depth/breadth

Table 4: Hyperparameters for the comparators

G.1 SINDy

The computational complexity for the SINDy algorithm is based on the Sequential Threshold Least Squares (STLS) process, and it is influenced by two main factors:

1. Number of library functions (q) — This refers to the number of candidate terms in the library, which is formed based on the polynomial degree and dimensionality of the system. In our case, we used polynomials at most degree 3 and we used 16, 32, and 128 dimensions of the Lorenz system.
2. Number of iterations (T) — The number of times the STLS algorithm iterates to threshold the coefficients. Each iteration performs regression on a progressively smaller set of terms after thresholding.

The complexity is derived by:

1. Sequential Thresholding: In each iteration, the algorithm identifies and zeroes out small coefficients (based on the threshold), which has complexity $O(qd)$, where q is the number of terms and d is the number of variables (or dimensions).
2. Least Squares Regression: After thresholding, the algorithm re-solves the least squares problem for the remaining large terms. The complexity of this operation depends on the size of the remaining set p , and it scales as $O(p^3)$, where $p \leq q$. In addition, as with our technique constructing the linear system is an $O(dNp^2)$ operation.

Hence, after each iteration, the algorithm refines the set of non-zero coefficients in the library, progressively reducing the number of terms included in the least squares regression.

Iterations

The number of iterations, T , can vary depending on the data and thresholding behavior. In general, T is relatively small compared to the size of the library, but it still affects the total complexity.

Overall complexity:

Given that the STLS algorithm iterates T times, the total computational complexity is $\mathcal{O}(T \cdot (qd + q^3 + dNq^2))$. The cubic and quadratic terms $\mathcal{O}(q^3 + dNq^2)$ dominate when solving the least squares problem, especially when the number of terms q is large, which is typical when higher-degree polynomials or large systems are considered.

G.2 Resnet

The Resnet algorithm use a residual network that learns the vector field. The input is a vector of dimension d . The output is also a vector of dimension d . There are q fully connected layers. The Resnet is trained during T epochs. The computational complexity is $\mathcal{O}(TNqd^2)$.

G.3 Latent ODEs

The Latent ODE model consists of two primary components: an encoder and a decoder. In the encoder, a set of ODEs is solved backward in time, where the ODEs operate on the observed state space of dimension d . In the decoder, the ODEs are solved forward in time, but they operate on a latent space of dimension q .

To compute the overall complexity of the algorithm, we define several key variables:

1. T : the number of epochs used to train the neural network,
2. k_1 : the total number of function evaluations (time points) used in the numerical solver for the encoder ODEs,
3. k_2 : the number of function evaluations for the decoder ODE,
4. n : the number of observed trajectories.

Given these notations, the per-epoch time complexity of the encoder is $\mathcal{O}(nk_1d^2)$, as the ODEs in the encoder are evaluated on a state space of dimension d . The per-epoch complexity of the decoder is $\mathcal{O}(nk_2q^2)$, as the ODEs in the decoder are evaluated on a latent space of dimension q .

Thus, the total per-epoch complexity of the model is:

$$\mathcal{O}(n(k_1d^2 + k_2q^2))$$

Finally, considering that the training runs for T epochs, the overall complexity of the algorithm becomes:

$$\mathcal{O}(nT(k_1d^2 + k_2q^2))$$

G.4 eDMD-Poly and eDMD-RFF

The complexity of the eDMD method can be expressed in terms of N : the number of training examples, q : the number of library functions, and d : the dimension of the data. We used a polynomial library for eDMD-Poly and random Fourier features for eDMD-RFF. The underlying algorithm was the same.

The first step is to evaluate the library functions on the training data, obtaining an (N, q) matrix Ψ . Next, we must numerically approximate the time derivatives of these quantities, yielding a matrix Ψ' . The complexity of these operations is $\mathcal{O}(Nq)$.

In the next step, we compute an approximation of the Koopman operator, given by $\mathcal{K} = \Psi^+ \Psi'$. The pseudoinverse has a complexity which depends on whether $N < q$ or $N \geq q$. In the former, the complexity is $\mathcal{O}(N^2q)$, while in the latter, it is $\mathcal{O}(Nq^2)$. The matrix-vector product $\Psi^+ \Psi'$ costs $\mathcal{O}(Nq^2)$ to compute.

Then we compute an eigendecomposition of \mathcal{K} , costing $\mathcal{O}(q^3)$. The eigenvectors correspond to approximate eigenfunctions of the true Koopman operator. Let E be the matrix of eigenvectors.

Let B be the matrix of coefficients of the full-state observable in terms of the library functions. This is a (d, q) matrix. The eigenmodes are thus given by BE^{-1} . The matrix E^{-1} can be expressed as the left eigenvectors of \mathcal{K} ; thus, it is computed during the eigendecomposition. Therefore, the eigenmodes only require multiplying (d, q) and (q, q) matrices together, costing $\mathcal{O}(dq^2)$.

The matrix B , if not computed analytically, may be computed by inverting a (q, q) matrix and performing d matrix-vector products, resulting in a complexity of $\mathcal{O}(dq^2 + q^3)$.

Thus, the total complexity is given by $\mathcal{O}((N+d)q^2 + N^2q + q^3)$ if $N < q$ and $\mathcal{O}((N+d)q^2 + q^3)$ if $N \geq q$.

The pseudoinverse step may be impractical in situations where there are many training examples. Thus, it may be substituted with a low-rank approximation using SVD. The rank of this approximation is a hyperparameter and will affect the complexity of the algorithm. We omit this consideration for the sake of simplicity.

G.5 eDMD-Deep

The eDMD-Deep method attempts to learn the library functions and the Koopman operator simultaneously. It does so by defining the library functions as the output of a neural network and minimizing the error incurred from a single Koopman operator update. Thus, the complexity is dependent on the architecture of the neural network used and the choice of optimizer.

Assume that optimization is done with stochastic gradient descent and the neural network outputs q library functions. Assume also that the data consists of n observations of d -dimensional trajectories. Suppose the neural network has L layers with q neurons each. Then a single iteration of SGD for the neural network has a cost of $\mathcal{O}(Ldq)$. Thus, an epoch has a cost of $\mathcal{O}(NLdq)$. Training for T epochs then costs $\mathcal{O}(TLNdq)$.

One must simultaneously optimize the cost function for the Koopman operator K , which is a (q, q) -dimensional matrix, with the neural network. Computing the gradient of the cost with respect to K requires multiplying a (q, q) matrix and q -dimensional vector, costing $\mathcal{O}(q^2)$. We compute this product for each item in the training set, costing $\mathcal{O}(Nq^2)$. Thus, the total cost of optimizing K over T epochs is $\mathcal{O}(TNq^2)$. Therefore, the cost of training the Koopman operator together with the library functions is $\mathcal{O}(TN(Ldq + q^2))$.

Once one has obtained the library functions and the matrix K , one proceeds as in eDMD and computes an eigendecomposition of K , followed by computing the eigenmodes, costing $\mathcal{O}(q^3 + dq^2)$. Thus, the complexity of the entirety of the eDMD-Deep algorithm is given by $\mathcal{O}(TN(Ldq + q^2) + dq^2 + q^3)$.

G.6 Runtime Results for the models

The theoretical runtimes of each benchmarked method is provided in figure 7. The experimental runtimes are also provided. The training and validation procedures differed for each of the methods making runtime comparisons difficult to interpret. Moreover, the hardware on which the models were run differed as well. For instance, all deep models were trained and run on GPUs while all other methods were not. In figure 7 we show the experimental runtimes for Lorenz96-16, Lorenz96-32 and Lorenz96-128 to give some suggestion as to how the runtimes scale as the dimension of the problem increases. The runtime of MOCK is not greatly impacted by the increase in the dimension.

The runtime for ResNet and Lode is quadratic in d (as can be seen in figure 7). In addition, eDMD-Poly and SINDy-Poly suffer from the problem that the number of polynomial features scales at least linearly with d . Thus these models scale at least cubically in d . q is determined by the user for eDMD-RFF and eDMD-Deep. If the user fixes q , then these methods will be linear in d . See the figure 7 and the discussion of G.6.

MOCK			ResNet			eDMD-Deep		
$\mathcal{O}(dN^3)$			$\mathcal{O}(kd^2TN)$			$\mathcal{O}(TN(Ldq + q^2) + dq^2 + q^3)$		
Data	val (h)	non-val (s)	Data	val (h)	non-val (s)	Data	val (h)	non-val (s)
L96-16	2.27	9.0	L96-16	.02	86.1	L96-16	5.63	62.34
L96-32	2.5	9.1	L96-32	.03	107.8	L96-32	4.58	81.3
L96-128	3.7	9.5	L96-128	.07	232.5	L96-128	6.8	123.9
eDMD-Poly			eDMD-RFF			Lode		
$\mathcal{O}((N + d)q^2 + N^2q + q^3)$			$\mathcal{O}((N + d)q^2 + q^3)$			$\mathcal{O}(nT(k_1d^2 + k_2q^2))$		
Data	val (h)	non-val (s)	Data	val (h)	non-val (s)	Data	val (h)	non-val (s)
L96-16	.31	7.0	L96-16	.08	1.56	L96-16	.23	829
L96-32	.43	8.1	L96-32	.08	1.6	L96-32	.44	1568
L96-128	.5	9.4	L96-128	.15	2.58	L96-128	4.7	16891
SINDy-Poly								
$\mathcal{O}(T(qd + q^3 + dNq^2))$								
Data	val (h)	non-val (s)						
L96-16	.1	1.4						
L96-32	.0025	1.5						
L96-128	.03	23						

Figure 7: val(h) is the training time including the training of the hyperparameters, in hours. non-val(s) is the training time excluding the training of the hyper-parameters, in seconds. For non-val, The MOCK algorithm scales most favorably with the dimension of the dataset, as increasing the dimension from 16 to 128 increases training time by less than 10%.